doi:10.26443/seismica.v5i1.1905

Tracking very low frequency earthquakes into long continuous records: application to the Southern Ryukyu subduction zone

Martin Vallée * [1], **Tanguy Delaporte** [1]

[1]Université Paris Cité, Institut de physique du globe de Paris, CNRS, Paris, France

Author contributions: *Conceptualization*: Martin Vallée. *Methodology*: Martin Vallée, Tanguy Delaporte. *Validation*: Tanguy Delaporte. *Formal Analysis*: Martin Vallée, Tanguy Delaporte. *Writing - Original draft*: Martin Vallée. *Writing - Review & Editing*: Tanguy Delaporte.

Abstract Very low frequency earthquakes (VLFEs) are generally absent from the standard seismicity catalogs because of their depleted seismic radiation at frequencies around and above 1 Hz. With the aim of improving their detection, we have developed an approach where the continuous three-component records of a station pair are first template-matched with the corresponding surface-wave time windows of previously known earthquakes. As a time delay is allowed for one of the stations of the pair, detected events may be not collocated with their templates, and their epicenters can be determined as soon as a second pair is considered. In a second stage, based on their high-frequency radiation, we determine whether the detected events are standard earthquakes absent from the template catalog or VLFEs. This two-stage method, referred as VLFE_DRL (VLFE Detection and Relative Location), is applied to the southern Ryukyu subduction zone where VLFEs were already known to occur. When compared with existing VLFE catalogs of the area, VLFE_DRL is shown to provide robust estimates of the VLFE source parameters. Between 2004 and 2024, VLFE_DRL detects and locates there more than 160 VLFEs with moment magnitude greater than 4, occurring in areas distinct from the standard interplate seismicity.

Production Editor:
Andrea Llenos
Handling Editor:
Marlon Ramos
Copy & Layout Editor:
Hannah F. Mark

Received:
August 5, 2025
Accepted:
February 26, 2026
Published:
March 15, 2026

1 Introduction

Most earthquakes follow on average well-established scaling laws, which in particular relate their source durations to their magnitudes. For such standard earthquakes, magnitude 5 earthquakes last no more than a few seconds while magnitude 7 earthquakes last no more than a few tens of seconds. Furthermore, the observed displacement spectrum of the P or S waves generated by these standard earthquakes is itself strongly controlled by the inverse of their duration, above which it follows a ω-square model (Aki, 1967). Some classes of earthquakes are, however, known to depart from this general behavior, with a longer duration and/or a lower high frequency content compared to what their moment magnitudes would predict. Among these are the so-called "Very Low Frequency Earthquakes" (VLFEs; Ishihara, 2003; Obara and Ito, 2005), that are usually missed by standard detection tools which require a clear P-wave signature at frequencies around or above 1Hz.

To be detected, VLFEs require analyses at lower frequencies (typically between 0.01 Hz and 0.05 Hz), most often using the surface waves that they generate. At the global scale, previous search for such anomalous earthquakes (Ekström, 2006; Poli, 2024) did not reveal large magnitude events: above moment magnitude $M_w \simeq 5$, the previously undetected events are either of non-tectonic origin (volcanic or glacial events, landslides) or in remote areas of the globe (mid-oceanic ridges in particular). In the latter case, their absence from the seismicity catalogs is at least partly due to the large distances to the nearest stations.

As mentioned by Ekström (2006), some moderate earthquakes (M_w between 4.5 and 5) absent from the National Earthquake Information Center (NEIC, Masse and Needham, 1989) or the International Seismological Centre (ISC, International Seismological Centre, 2024) catalogs are, however, located offshore Japan, close to a very well instrumented area. This source location is consistent with the early VLFE detections of Ishihara (2003) in the Nankai subduction zone. Another puzzling location shown by the global studies of Ekström (2006) and Poli (2024) is the southern Ryukyu subduction zone, close to Taiwan. In the last fifteen years, several studies confirmed that VLFEs are abundant both in the Ryukyu (e.g., Ando et al., 2012; Nakamura and Sunagawa, 2015; Nakamura and Yakabu, 2025) and Nankai (e.g., Nakano et al., 2018; Takemura et al., 2023, and references therein) subduction zones. In both areas, their moment magnitudes M_w were shown to reach 4.5–5. VLFEs were also detected in the Japan trench, in particular offshore Tokachi (Asano et al., 2008). Lower magnitude VLFEs were also found in the Mexico (Maury et al., 2016) and Costa Rica (Baba et al., 2021) subduction zones. In the Cascadia subduction zone, VLFEs were first identified with a M_w range between 2.2 and 4.1 (Ghosh et al., 2015; Ide, 2016; Hutchison and Ghosh,

*Corresponding author: vallee@ipgp.fr

2016), but a much larger event ($M_w = 5.7$) was recently detected in the minutes following a large teleseismic event (Fan et al., 2022). In contrast, today VLFEs remain undetected in very active subduction zones, such as Alaska or the whole margin of South America.

In subduction zones, the abovementioned studies have shown that VLFEs most often have a mechanism consistent with reverse slip on the plate interface. Their locations are found adjacent to the seismogenic zone, at larger depth (Cascadia, Mexico), at shallower depth (Ryukyu, Costa Rica, Japan trench), or at both shallower and larger depths (Nankai). They are thus observed in areas between locked and stable sliding zones, and even if their exact mechanisms remain uncertain and debated, VLFEs are widely viewed as manifestations of this transitional fault zone stability (Saffer and Wallace, 2015). Slow slip can also be expressed by the larger magnitude Slow Slip Events (SSEs), with typical duration of days to months and whose detection can only be done geodetically; and by the lower magnitude Low Frequency Earthquakes (LFEs), whose detection requires local observations. The recurrent activity of LFEs is a likely explanation for the tremors observed in a number of subduction zones (Shelly et al., 2007). More generally, all these phenomena can be interpreted as being part of the same process (Ide et al., 2007; Peng and Gomberg, 2010), with the large magnitude SSEs driving the other low frequency deformation processes (e.g., Nakamura and Sunagawa, 2015; Nakano et al., 2018). In this view, VLFEs appear to be valuable slow slip detectors, because they are potentially observable at much further distances than both SSEs and LFEs.

The scope of this study is to build a method for systematic VLFE detection at regional distances, using the past seismicity as a template. Compared to analyses previously done at global scale (Ekström, 2006; Poli, 2024), the magnitude detection threshold can be significantly lowered. Besides the potential of finding new VLFE areas, the decades-long operation of broadband seismometers (from the global or local networks) also enables characterization of the VLFE activity in an exhaustive way. This is required to determine their frequency-magnitude distribution, whose differences with the one of the standard earthquakes has been little studied.

We first introduce the VLFE Detection and Relative Location (VLFE_DRL) method, before detailing its implementation in the southern Ryukyu subduction zone. We then present how the VLFE_DRL method is able to find both standard and very low frequency earthquakes that are located in the vicinity of the templates. The characteristics of the detected VLFEs, including their magnitude distribution, will then be examined and discussed.

2 VLFE_DRL method

2.1 General strategy

The general idea of this approach is to use the existing seismicity catalogs in order to detect and characterize other events that share similarities in their low frequency wavefield but may differ in terms of location and frequency content. Each of the known earthquakes will be referred as a template, and the search for events similar to these templates is done on the continuous waveforms of a few stations located at regional distances (from one hundred kilometers to two thousand kilometers) from the targeted area. The low number of required stations enables us to explore even low-instrumented regions of the globe. When using surface waves in a frequency band between 0.01–0.02 Hz and 0.03–0.05 Hz, this typically allows the association of new earthquakes down to M_w = 3.5–4. New associated events have a similar mechanism and depth compared to their templates, and waveform scaling provides their relative seismic moment. As soon as three stations can be used, an estimate of the event location relative to the template can be determined. The second stage of the VLFE_DRL method compares the high frequency content of the associated events, in order to determine if some of them are VLFEs.

2.2 Template matching detection using station-pair differential times

Given a template earthquake i with known location, seismic moment M_0^i, and origin time T_0^i, we note τ_k^i the travel time and t_k^i ($t_k^i = T_0^i + \tau_k^i$) the arrival time of the waves of interest at station k. We also note $S_k^l(t_k^i)$, the l component of the velocity signal recorded at station k, bandpass filtered between frequencies f_h and f_l, and windowed around t_k^i. The windowing is only done such that all the targeted wavetrain (and only it) is well recorded, which does not require the exact knowledge of t_k^i. The chosen values of f_h and f_l are application-dependent, with the constraint that f_l is lower than the corner frequency of the earthquakes we aim to detect. The template signal $S_k(t_k^i)$ is defined as the concatenated signals over the 3 components of station k :

$$S_k(t_k^i) = \left[S_k^1(t_k^i)\ S_k^2(t_k^i)\ S_k^3(t_k^i)\right] \tag{1}$$

This concatenation is equivalent to the approach proposed by Yang et al. (2009), who define the template and continuous signals as three-component vectors and then use their dot product in the correlation operations. Such template forms are useful both to take into account that a given wave may have low amplitude over one or two of the signal components and to enforce the focal mechanism similarity of the detected events.

Following template matching techniques (e.g., Gibbons and Ringdal, 2006; Shelly et al., 2007; Peng and Zhao, 2009; Tang et al., 2010, and references therein), we consider, for all times t, the correlation coefficient c_k^i between the time-shifted windowed continuous records and the template signal:

$$c_k^i(t) = \mathbf{Cor}\left(S_k(t + t_k^i)\ ,\ S_k(t_k^i)\right) \tag{2}$$

where $\mathbf{Cor}$ is the Bravais-Pearson correlation coefficient. Classical techniques then search the local maxima of the c_k^i stack for all the available stations k. Here, we first use two stations (e.g. $k = 1, 2$) and define an average correlation coefficient C_{12}^i, depending both on

t and on a delay dt:

$$C_{12}^{i}(t,dt)=\frac{c_1^i(t)+c_2^i(t+dt)}{2} \tag{3}$$

As will be made clear below, dt values are physically bounded between a lower bound $\widehat{dt}_{12}^{i}$ and an upper bound $\breve{dt}_{12}^{i}$. For $dt\in[\widehat{dt}_{12}^{i}\ \breve{dt}_{12}^{i}]$, we extract all the couples $((t^j,dt_{12}^{ij}),j=1,N)$ corresponding to local maxima C_{12}^{ij} (above a given threshold $\widehat{C}_{12}$) of function C_{12}^{i}. We can also impose that the individual correlations $c_1^i(t^j)$ and $c_2^i(t^j+dt_{12}^{ij})$ are both above a given threshold $\widehat{c}_{12}$. Each event j is termed member of the family associated with template i. Detection time t^j verifies the two equations :

$$\begin{cases} t^j+t_1^i=t_1^j \\ t^j+t_2^i+dt_{12}^{ij}=t_2^j \end{cases} \tag{4}$$

The seismic moment M_0^j can be estimated from the amplitude ratios :

$$M_0^j=M_0^i\,\frac{\mathcal{A}(S_1(t^j+t_1^i))}{\mathcal{A}(S_1(t_1^i))}=M_0^i\,\frac{\mathcal{A}(S_2(t^j+t_2^i+dt_{12}^{ij}))}{\mathcal{A}(S_2(t_2^i))} \tag{5}$$

where $\mathcal{A}$ is an amplitude measurement of the signal, for example its standard deviation or the difference between its extreme values. The consistency between the two amplitude ratios can also be used as an additional criterion to keep or remove the obtained detection. If the j event has a corner frequency f_c^j close to f_l, its seismic moment derived from equation (5) is expected to be underestimated. As f_c^j is the frequency where the displacement amplitude drops below the half-value of the low frequency limit, this underestimation may reach 0.2 units in terms of moment magnitude.

Using system (4), the arrival times t_1^j and t_2^j of event j at stations 1 and 2, respectively, are related to the values of t_1^i, t_2^i and dt_{12}^{ij} by :

$$dt_{12}^{ij}=(t_2^j-t_1^j)-(t_2^i-t_1^i)=(t_2^j-t_2^i)-(t_1^j-t_1^i) \tag{6}$$

This equation shows that dt_{12}^{ij} can be seen as the double-pair differential arrival time, from the two events j and i at the two stations 1 and 2 (Guo and Zhang, 2016). Here, this quantity will be used both for detection and location, and not only for relocating already known earthquakes. This objective is therefore similar to the Match and Locate method of Zhang and Wen (2015) and to the SCC method of Yang et al. (2009), with practical differences that will be discussed in section 2.3. Writing equation (6) in terms of travel times, we obtain :

$$dt_{12}^{ij}=(\tau_2^j-\tau_2^i)-(\tau_1^j-\tau_1^i) \tag{7}$$

When the detected event j is both further to station 1 and closer to station 2 than template i, dt_{12}^{ij} takes large negative values. When the detected event j is both closer to station 1 and further to station 2 than template i, dt_{12}^{ij} takes large positive values. In real applications of the method, a maximum inter-event distance R^i (between i and j), for which event j can be associated to event i in a meaningful way, will be predefined. This value of R^i will be used to estimate, with synthetic travel times, the $\widehat{dt}_{12}^{i}$ and $\breve{dt}_{12}^{i}$ bounds mentioned above.

When using high values of $\widehat{C}_{12}$, this station-pair technique is a powerful detector of events similar to template i, located in its vicinity. A simultaneous high correlation on two $\times$ three components, respecting a physical delay between the two stations, is unlikely to occur in the background seismic wavefield or for events outside the targeted area. However, for lower values of $\widehat{C}_{12}$, the latter possibility becomes possible: spurious correlation between different wave types at stations 1 and 2 may occur and even if the same wave types are correlated, a low $|dt_{12}^{ij}|$ value does not imply that the detected event j is close to the template i.

2.3 Event confirmation and surface wave location

The use of a third station ($k=3$) first increases the confidence in the actual detection of neighboring events. If we find, with the pair of stations 1 and 3, a local maximum C_{13}^{ij} of C_{13}^{i} larger than $\widehat{C}_{13}$ for the time t^j and for a delay $dt_{13}^{ij}\in[\widehat{dt}_{13}^{i}\ \breve{dt}_{13}^{i}]$, event j is also detected by the pair 1-3. The quality of the common detection can be evaluated by $\bar{C}^{ij}=(C_{12}^{ij}+C_{13}^{ij})/2$. The third station also enables another relative seismic moment measurement as in equation (5). Furthermore, the delays now verify the two equations:

$$\begin{cases} dt_{12}^{ij}=(\tau_2^j-\tau_2^i)-(\tau_1^j-\tau_1^i) \\ dt_{13}^{ij}=(\tau_3^j-\tau_3^i)-(\tau_1^j-\tau_1^i) \end{cases} \tag{8}$$

Each equation constrains the event j to be on a surface (hyperboloid in an homogeneous medium). If R^i is also chosen significantly smaller that the distance from i to all stations, the station azimuths θ_1^i, θ_2^i and θ_3^i can be considered to be the same for i and j. With the further assumption of a constant phase velocity V_ϕ in the source region, the travel times delays $(\tau_k^i-\tau_k^j)$ are linearly dependent on the Cartesian coordinates of the j event with respect to the i template (Frechet, 1985). In this study, we will restrict our analysis to surface waves (horizontal take-off angle), in which case we have for example for station 1:

$$\tau_1^i-\tau_1^j=\frac{x^j\sin\theta_1^i+y^j\cos\theta_1^i}{V_\phi} \tag{9}$$

where x^j (East) and y^j (North) are the coordinates of event j relative to template i. The system (8) can thus be written:

$$\begin{cases} x^j(\sin\theta_1^i-\sin\theta_2^i)+y^j(\cos\theta_1^i-\cos\theta_2^i)=V_\phi\,dt_{12}^{ij} \\ x^j(\sin\theta_1^i-\sin\theta_3^i)+y^j(\cos\theta_1^i-\cos\theta_3^i)=V_\phi\,dt_{13}^{ij} \end{cases} \tag{10}$$

The determinant of the system for x^j and y^j is equal to:

$$4\sin\left(\frac{\theta_1^i-\theta_2^i}{2}\right)\sin\left(\frac{\theta_1^i-\theta_3^i}{2}\right)\sin\left(\frac{\theta_2^i-\theta_3^i}{2}\right) \tag{11}$$

If (and only if) the three azimuths are all different, x^j and y^j are thus uniquely determined by the standard resolution of the linear system. The use of more stations, all with different azimuths, would lead to on overdetermined system which can then be solved in terms of least square optimization. Alternatively, the

phase velocity V_ϕ can also be optimized if using three or more station pairs. Redundant pairs (e.g. the 2-3 pair in the case of three stations) can also be considered with the goal to improve the location robustness. However, this makes the association criterion more difficult because C^i_{23} is not expected to have a local maximum for time t^j. In the first application of the method, we will remain in the configuration of solving system (10).

This goal of simultaneous detection and location of non-collocated events by multi-station template matching has already been achieved by the Match and Locate (M&L) method of Zhang and Wen (2015). In this approach, all the individual c^i_k correlations for each station k are stored, and the volume around the template is discretized into a large number of potential sources. At each time t and for each potential source, a c^i_k stack is then computed using the expected station-dependent delays. Events are therefore simultaneously detected and located when and where the four-dimensional stacks reach a significant threshold. Uncertainties on the obtained locations can also be derived. Compared to our approach, M&L has the advantage that the delays do not have to be linearly related to the relative event coordinates, as in equation (9). Its main drawback is that events are detected and located only after having tested all the possible grid points, which is much longer than the standard resolution of a low-dimension linear system.

In the two-step SCC method of Yang et al. (2009), events are first detected using their correlations with known templates at a single station (the one with strongest detection power, typically the closest one from the templates). Their arrival delays at all stations are then measured by cross-correlation and events are relocated with the double-difference method of Waldhauser and Ellsworth (2000). The method developed here should therefore provide similar results, but with the advantage that detection and location are done simultaneously. Furthermore, the first step of SCC is expected to be more sensitive to spurious detections (that need to be rejected in the second step), as correlations are made with a single station and not with station pairs.

2.4 Identification of very low frequency earthquakes

An associated event j is similar to the template i in terms of focal mechanism, depth, and frequency content up to f_l. The analysis of higher frequencies is most easily done on the waves with the highest frequency content, i.e. P waves. The P arrival time t^i_{Pk} of template i at station k can be computed with an accuracy of less than a few seconds. There is more uncertainty on t^j_{Pk} because we do not know the precise value of T^j_0. We therefore use $t^j_{Pk} = t^j + t^i_{Pk}$, which does not take into account the location difference between i and j. This information is, however, sufficient to extract the P wave time window for each associated j event.

We note $a^j(t)$, the acceleration signal filtered between f_1 and f_2. f_1 is chosen higher than the highest corner frequency of all the events (and then in particular higher than the corner frequency f^j_c of the j event). f_2 is chosen below the frequency where amplitudes tend to be reduced due to attenuation. $a^j_P(t)$ is the $a^j(t)$ signal windowed in the P wave time window. In the ω-square model (Aki, 1967), the amplitude A^j of the $a^j_P(t)$ spectrum is constant and proportional to:

$$A^j \propto M^j_0 (f^j_c)^2 \tag{12}$$

On the other hand, according to earthquake scaling laws (e.g., Boore, 1983):

$$M^j_0 \propto \Delta\sigma^j (f^j_c)^{-3} \tag{13}$$

where $\Delta\sigma^j$ is a proxy for the stress drop of event j, as a slow rupture velocity or a low slip rate also results in a low value of $\Delta\sigma^j$. Taking into account this limitation, the stress drop term will be kept for $\Delta\sigma^j$ in the remainder of the study. Eliminating the unknown value of f^j_c using equations (12) and (13), we have:

$$\Delta\sigma^j \propto \sqrt{\frac{(A^j)^3}{M^j_0}} \tag{14}$$

The stress drop variability can also be visualized from the acceleration time history. Using Parseval theorem, and noting $\overline{(a^j_P(t))^2}$, the average of the squared acceleration values, we have:

$$\frac{\overline{(a^j_P(t))^2}}{(M^j_0)^{2/3}} \propto \frac{(A^j)^2}{(M^j_0)^{2/3}} \propto (\Delta\sigma^j)^{4/3} \tag{15}$$

For the N associated events with a template i, we call m_i the event with the largest stress drop, and compute from (14) the relative stress drop value $\Delta\sigma^j_{m_i}$ for each j associated event (see also Walter et al., 2017):

$$\Delta\sigma^j_{m_i} = \sqrt{\left(\frac{A^j}{A^{m_i}}\right)^3 \frac{M^{m_i}_0}{M^j_0}} \tag{16}$$

$\Delta\sigma^j_{m_i}$ is thus bounded between 0 and 1. The lowest value is in practice bounded by the high-frequency noise relative to the measured amplitudes, and the analysis is thus best conducted at the quietest of the close stations. Inside the family associated with template i, $\Delta\sigma^j_{m_i}$ is expected to show some variability even when the associated events are all standard earthquakes. First, the stress drop $\Delta\sigma^j$ is known to vary even for neighboring and similar earthquakes (Allmann and Shearer, 2009; Chounet and Vallée, 2018) as a result of the complicated rupture dynamic process. It may also be practically difficult to analyze frequencies high enough so that equation (12) is exact. As a consequence, a slight tendency of larger $\Delta\sigma^j_{m_i}$ for larger earthquakes is likely. Finally, as the j event may be not collocated with the m_i event, $\Delta\sigma^j_{m_i}$ may differ from 1 even when the stress drops are the same.

VLFEs, with little or no observed radiation in the P wave time windows, are expected to be well outside this variability and will be detected by the abnormally low values of $\Delta\sigma^j_{m_i}$. For a detected VLFE j, its real stress drop ratio with respect to event i may be even smaller than the one given by equation (16), because its seismic moment M^j_0 may have been underestimated (see section 2.2).

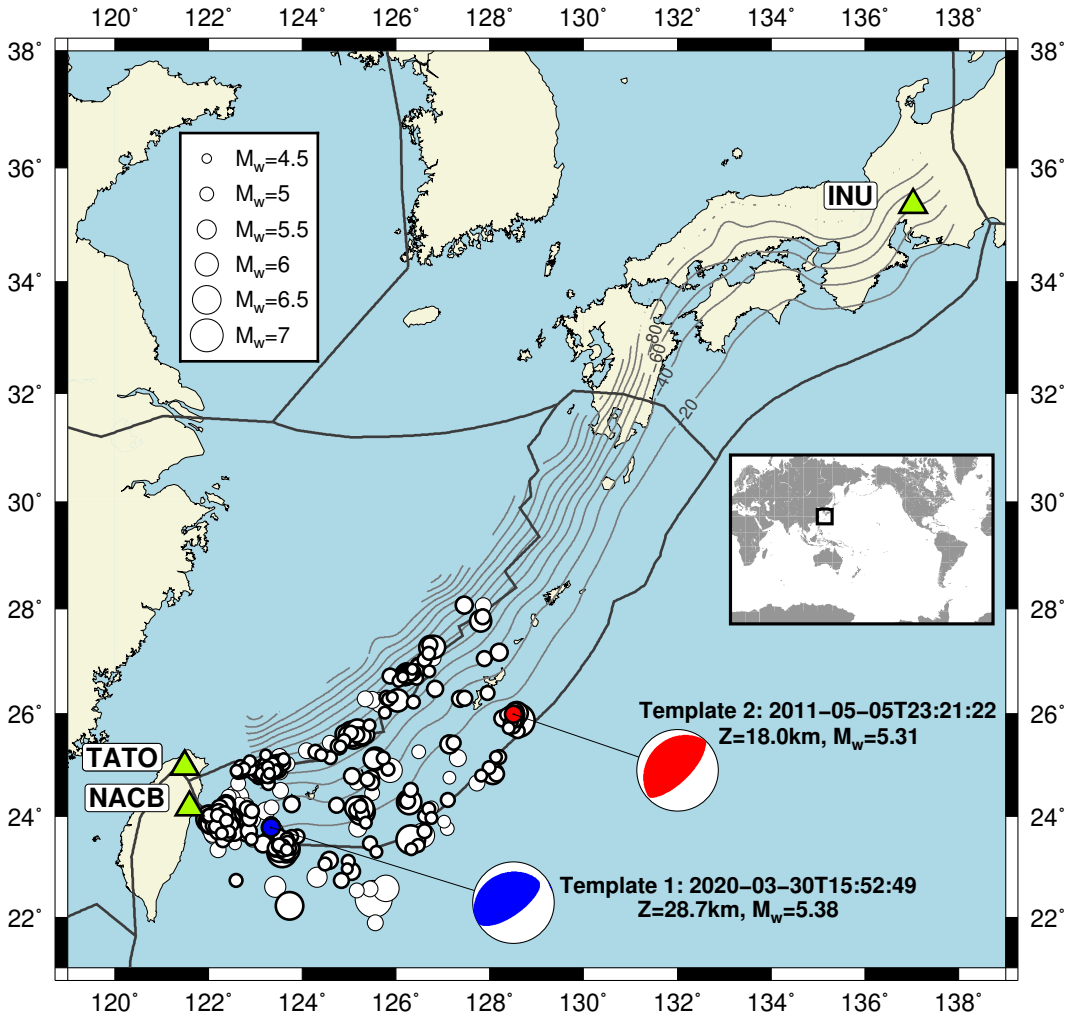

Figure 1 Map of stations and templates. The three stations considered (TATO, INU, NACB) are shown by green-filled triangles. Templates recorded by the TATO-INU pair and by the TATO-NACB pair are shown by white circles with thin and thick contour, respectively. Circles size is scaled to template moment magnitude, ranging between 4.58 and 7.44. For further illustration of the procedure, two templates are highlighted in blue and red, and shown with their focal mechanism, origin time, depth, and moment magnitude. All the information about template locations, moment magnitudes, and focal mechanisms comes from GCMT (Ekström et al., 2012). Thick grey lines are the plate boundaries according to Bird (2003). Thin grey lines are the isodepth contours (every 20 km) of the Ryukyu slab according to the Slab1.0 model (Hayes et al., 2012).

3 Application to the Southern Ryukyu subduction zone

3.1 Data selection and processing

Our goal is to select high-quality broadband stations, with easy access to long recording times, located at regional distances from the southern Ryukyu subduction zone. The three selected stations (Figure 1) are TATO in Taiwan (GSN/IU network, Albuquerque Seismological Laboratory/USGS, 1988), INU in Japan (Geoscope/G network, Institut de physique du globe de Paris (IPGP) and École et Observatoire des Sciences de la Terre de Strasbourg (EOST), 1982) and NACB in Taiwan (BATS/TW network, Institute of Earth Sciences, Academia Sinica, Taiwan, 1996) . TATO, INU and NACB provide continuous access to their LH? channels (1 Hz sampling) since 1992, 1988 and 2004, respectively. The station pair TATO-INU (k=1, 2) therefore offers more than 30 years of continuous common operation. At high frequency (above 1 Hz), NACB station (k=3) is quieter than TATO, which helps the final detection of VLFEs (section 2.4). The continuous records are retrieved using standard webservices interfaces (see Open Research section) and cut in common ≃5-day-long time windows.

As a template catalog, we use GCMT (Ekström et al., 2012). All the shallow earthquakes (shallower than 60 km depth) located, with respect to the TATO station, at epicentral distances between 1° and 6.5° and at back-azimuths between 10° and 160°, are considered (Figure 1). For the TATO-INU pair (years 1992-2023), this results in 361 templates jointly recorded by the two stations. For the TATO-NACB pair (years 2004-2023), this results in 307 templates jointly recorded by the two stations. For templates i in the eastern part of the target area, the observation geometry is not expected to be ideal for accurate relative location, because θ_1^i and θ_3^i are close. This is, however, not the main goal of the present study, where we first aim to detect and quantify abnormal high-frequency contents between nearby events.

Both continuous and template waveforms are con-

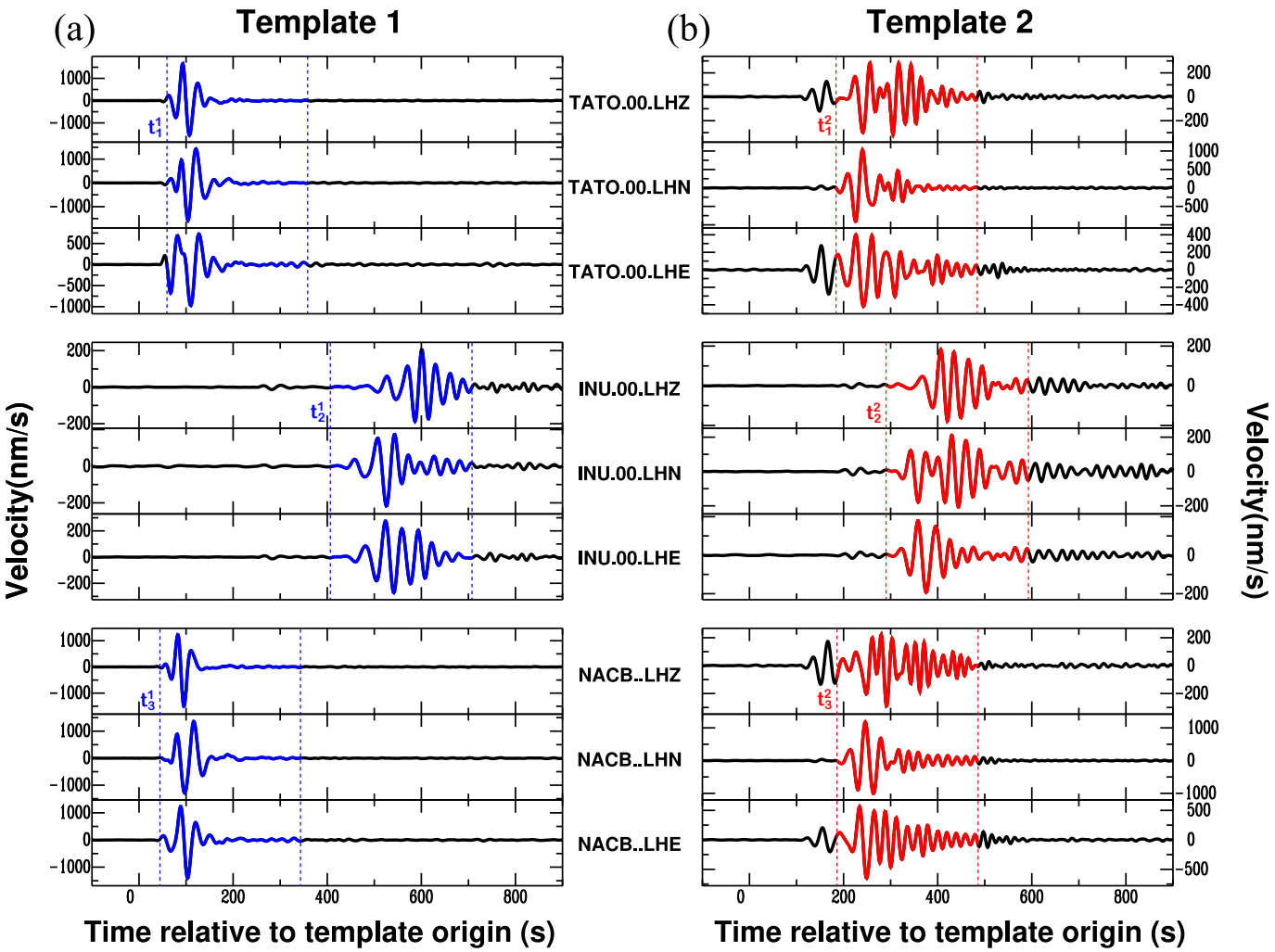

Figure 2 Illustration of windowed waveforms for two templates. Template 1 (a) and Template 2 (b) are earthquakes whose location and characteristics are shown in Figure 1. Their windowed waveforms, extracted from the continuous waveforms (in black) of the three components of the three stations (TATO, INU and NACB), are shown in blue (Template 1) and in red (Template 2). Each of the colored waveforms thus corresponds to the term $S_k^l(t_k^i)$, for the three stations ($k = 1, 3$), the three components ($l = 1, 3$) and 2 templates ($i = 1, 2$).

verted to velocity using the instrumental response, and horizontal components are rotated along the North and East components. All three components are then filtered between $f_h = 0.0125$ Hz and $f_l = 0.03$ Hz. In this frequency band, the noise level is low and events with similar mechanisms and locations are expected to be well correlated as soon as their source durations are shorter than a few tens of seconds. Furthermore, for shallow events, one wave type (surface waves) dominates the records (Figure 2), which makes the windowing process non-critical (section 2.2). As illustrated in Figure 2 for two representative templates (whose location and characteristics are shown in Figure 1), selected waveforms are 300-second-long distance-dependent windows for each component, that well include the surface wave packets. We show in Figure 3 how INU and TATO waveforms are then concatenated in order to build the 900-second-long template signals $S_1(t_1^1)$ and $S_2(t_2^1)$.

3.2 Implementation

The maximum inter event distance R^i is defined according to the empirical relation $R^i = \min(0.3r^i, 100)$, where r^i is the distance between template i and TATO station (all distances in km). This relation takes into account that, for a given distance to a template, events are less and less likely to be associated if the template is closer to one of the stations. Using R^i and an average surface wave velocity of 3.8 km/s, the $\check{dt}^i_{12}$, $\hat{dt}^i_{12}$, $\check{dt}^i_{13}$ and $\hat{dt}^i_{13}$ bounds are computed for each template i. As a consequence of the large chosen value for R^i and of the small chosen value for the average surface wave velocity (considering surface waves in the 0.0125 Hz–0.03 Hz frequency range), meaningful detections are expected to be rare outside these bounds. The correlation thresholds $\widehat{C}_{12}$ and $\widehat{c}_{12}$ (TATO-INU pair) are respectively set to 0.76 and 0.7 whereas the correlation thresholds $\widehat{C}_{13}$ and $\widehat{c}_{13}$ (TATO-NACB pair) are respectively set to 0.8 and 0.7. This difference takes into account that a high correlation value is easier to reach for pairs with similar event-station paths.

The detection search is done sequentially for each

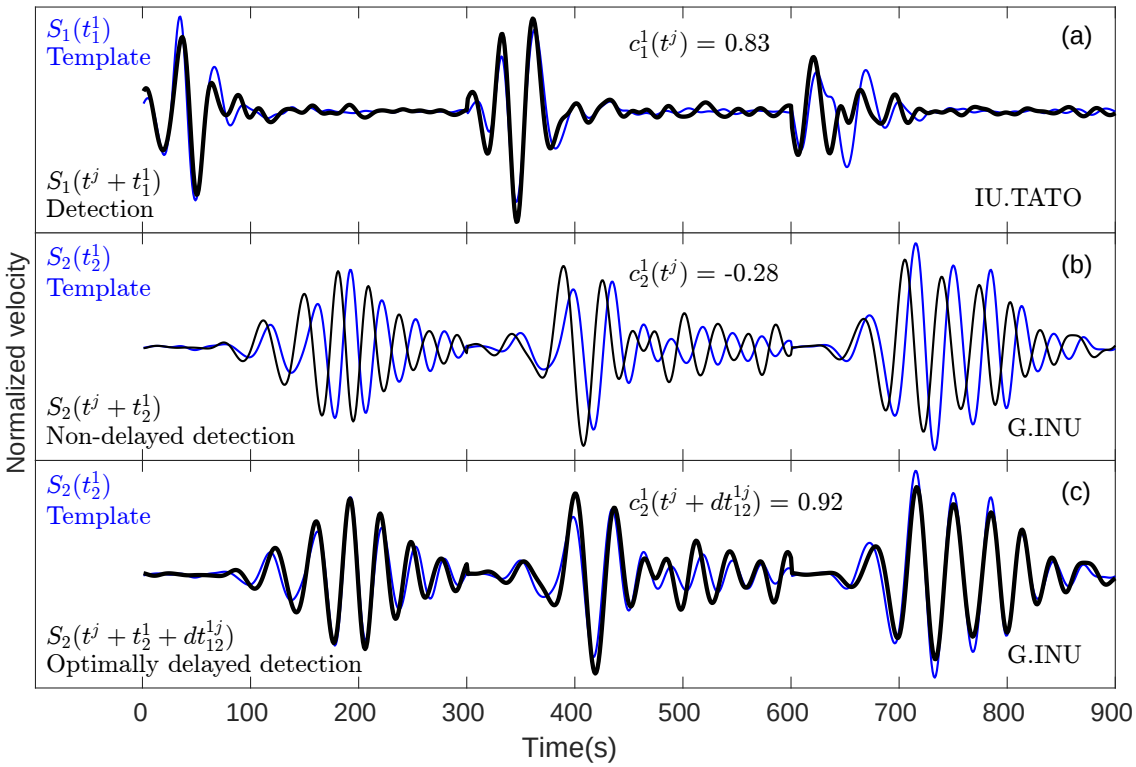

Figure 3 Example of an event j detected thanks to the high values of C_{12}^{1j}. Event j occurred on 2005/06/01T11:53:30 and will be shown to be a VLFE (see Supplementary Table S1). In (a), (b) and (c), waveforms of Template 1 (see also Figures 1 and 2) are shown in blue and windowed waveforms of event j are shown in black. In (a) and (c), that highlight the interest of the method used here, the windowed waveforms of event j are shown in bold. All waveforms have been normalized using their standard deviations. (a) shows the event waveforms at station 1 (TATO) for the optimal detection time t^j, corresponding to the local maximum of c_1^1 here equal to 0.83. (b) shows the event waveforms at station 2 (INU) for the same detection time t^j, thus assuming that template and event occurred at the same place (standard template matching). Cross-correlation coefficient $c_2^1(t^j)$ takes a low value of -0.28. (c) again shows the event waveforms at station 2 (INU), but for the detection time t^j optimally corrected by dt_{12}^{1j}, in order to maximize C_{12}^{1j}. dt_{12}^{1j} is here equal to -11 s and the $c_2^1(t^j + dt_{12}^{1j})$ correlation coefficient is now equal to 0.92. If using standard template matching techniques that maximize $(c_1^1 + c_2^1)/2$, the optimal average correlation would peak at 0.48 (for $t = t^j - 5$), much lower than the 0.88 C_{12}^{1j} value obtained here.

of the common ≃5-day-long continuous time windows, using, for all possible templates, a discrete version of equation 3 where times t and dt are sampled each second. This process is easily parallelized as correlation computations at a time t and for a template i are independent of other times and other templates.

Figure 3 shows an example of detection by the 1–2 (TATO-INU) pair of an event j associated with Template 1, that strongly benefits from the dt delay included in function C_{12}^i. C_{12}^{ij} indeed reaches 0.88 for the optimal detection time t^j and delay dt_{12}^{1j}, while it would only peak to 0.48 for the correlation stack function $(c_1^1+c_2^1)/2$. Detecting such an event with standard template matching techniques would therefore require to strongly reduce the correlation threshold, with the consequence of increasing the number of false detections, in particular when only few stations are available. Figure 3 also shows how regional waveforms in the chosen frequency range remain highly correlated even for events whose location significantly differs from the one of the template. In the present case, the dt_{12}^{1j} value of -11 s implies that the event is at least ≃30 km away from the template (the complementary use of the TATO-NACB pair shows that it is in fact more than 40 km away). This illustrates the long action range of a template in terms of event association.

For each template i, events j jointly detected by the two pairs are located by using their station-pair differential arrival times dt_{12}^{ij} and dt_{13}^{ij}, and inverting system (10). In practice, as the station-pair differential arrival times are sampled each second, we take into account the associated uncertainty by randomly adding values between -0.5 s and 0.5 s to dt_{12}^{ij} and dt_{13}^{ij}. In this system, V_ϕ is taken equal to 4.15 km/s. This value takes into account that the waveforms are dominated by frequencies close to the upper bound of the selected frequency range (0.03 Hz). At such frequencies, according to the values of the GDM52 model (Ekström, 2011) in the southern Ryukyu subduction zone, the selected phase velocity lies in between the Rayleigh waves (≃3.9 km/s) and Love waves (≃4.4 km/s) phase velocities. For the long-running TATO-INU pair, all detection times t^j and associated dt_{12}^{ij} are also kept, even in absence of joint detection by the TATO-NACB pair.

Events are frequently detected, quantified in terms of seismic moment, and relatively located by more than one template. In this case, it is both interesting to consider the information brought by the best-correlated

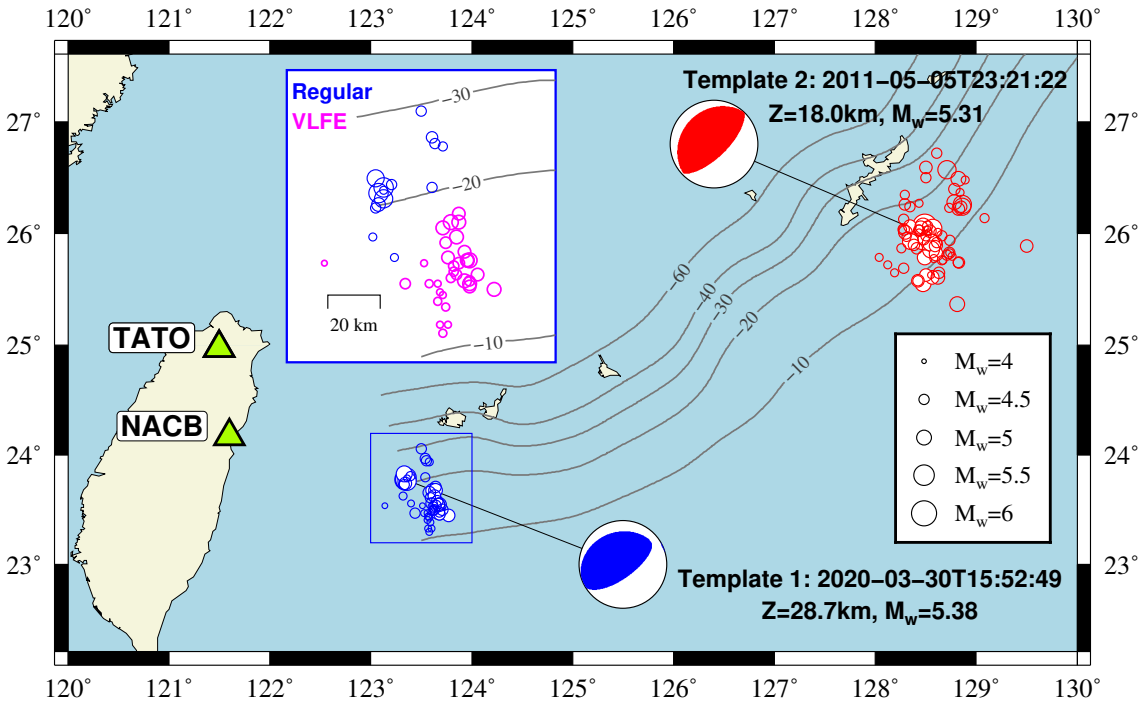

Figure 4 Relative location and magnitude of the events detected by Template 1 (blue) and by Template 2 (red), using TATO, INU and NACB stations. Focal mechanism, depth and M_w magnitude of Template 1 and Template 2 are from GCMT. Circles size is scaled to events moment magnitude (see main text), which ranges between 4.05 and 5.87. White-filled circles correspond to re-detected templates. In the blue inset, the events detected by Template 1 and identified as VLFEs are shown in magenta and the other ones (regular earthquakes) are shown in blue. Thin grey lines are isodepth contours of the Ryukyu slab according to the Slab1.0 model (Hayes et al., 2012).

template (by means of C_{12}^{ij} or $\bar{C}^{ij}$) and to keep the template-dependent information. The former case provides a global view of the detected events in the target area. The latter case is more adapted to study the spatial organization of the events inside a family. Inside such a family, the possible presence of other known templates is useful for redundant moment estimates.

For all the detected events, the vertical P-wave windows are retrieved at a higher sampling (20 Hz, BHZ channel), using the same request tools as for the continuous records. For events located by the two pairs, the quiet NACB station is selected. For events only detected by the TATO-INU pair, the TATO station is selected, and we only consider the events j detected by templates i with C_{12}^{ij} larger than 0.8. The second stage of the VLFE_DRL method described in section 2.4 is then applied inside each template family to detect abnormal high-frequency content. The NACB station enables working in the 3–5 Hz frequency range, therefore at a higher frequency than the corner frequency of $M_w = 4$ standard earthquakes (typically from 1 to a few Hz). The moment dependency of the measurements is therefore expected to be smaller than for the TATO station, where we are constrained to work in the 2–4 Hz frequency range. Furthermore, the higher noise level of the TATO station may prevent detection of VLFEs, when the high-frequency P waves of standard earthquakes are not high enough above this noise level.

4 Very low frequency earthquakes and regular earthquakes in the Southern Ryukyu subduction zone

4.1 Examples of detection of very low frequency earthquakes

Figure 4 shows all the events detected by two illustrative templates (see their waveforms in Figure 2) and located in reference to them. All the events shown on the map therefore occurred between 2004 and 2024, when the TATO, INU, and NACB stations are running together. White-filled events are templates (either the one used for detection or other known templates). For each of the three stations, we average the magnitudes derived from each of these templates (using their GCMT magnitudes), and then select the median of the three values. By doing so, magnitudes are obtained in a consistent way for all the events of the family, and the obtained values are more robust than if we only rely on the magnitude of the template used for detection. For Template 1, among the 49 events jointly detected by the two station pairs, 37 events are not in the GCMT catalog (11 known templates are therefore detected in addition to Template 1 itself). For Template 2, among the 78 events jointly detected by the two station pairs, 61 events are not in the GCMT catalog (16 known templates are therefore detected in addition to Template 2 itself). Events magnitude ranges between 4.05 and 5.38 for detections made by Template 1 and between 4.19 and 5.87 for detections made by Template 2.

Figure 5 shows the vertical records in the P wave win-

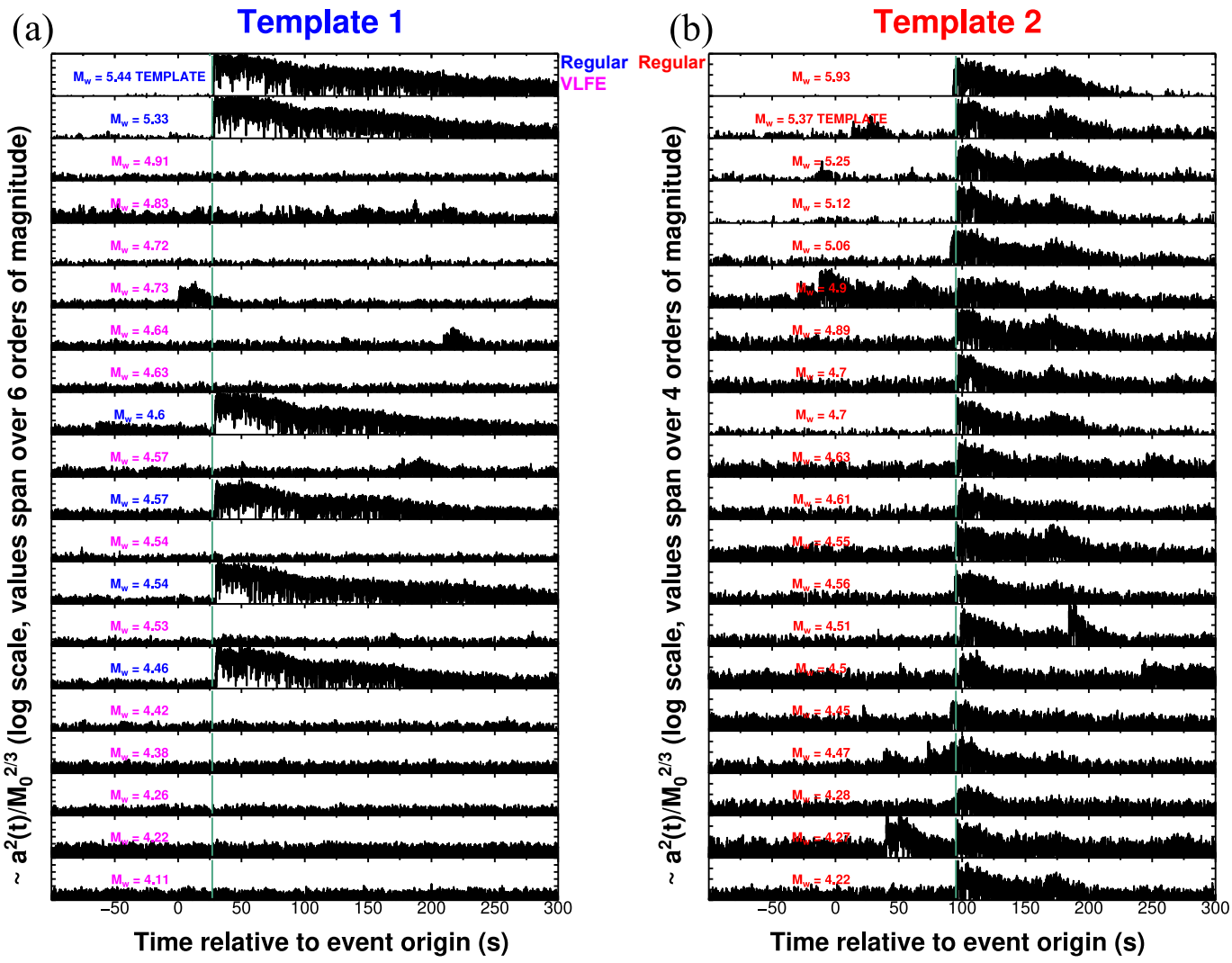

Figure 5 High-frequency records of events belonging to the same template family. (a) A random subset of 20 events (among a total of 49 events) detected by Template 1 is selected, and corresponding vertical waveforms recorded at NACB are ordered by decreasing magnitude (M_w) from top to bottom. The waveform corresponding to the template itself is identified by the word added to the right of the magnitude value. Each waveform is converted to acceleration, bandpass filtered between 3 Hz and 5 Hz, squared, and scaled to the event seismic moment to the power $2/3$. The green vertical bar corresponds to the expected P arrival. Records corresponding to VLFEs (identified by their $\Delta\sigma^j_{m_1}$ below 0.01) have their magnitude written in magenta. They all show an obvious depletion in high frequencies. These VLFEs are shown in the map inset of Figure 4 with this same magenta color. Records corresponding to regular earthquakes have their magnitude written in blue. (b) Same as (a) for Template 2 (the total number of detected events is 78 in this case). P waves always have a similar amplitude once corrected from the seismic moment dependency; all detected events are thus categorized as regular earthquakes and labeled with the same color (red).

dow, at NACB station, for a random subset of 20 events belonging to Template 1 family (Figure 5a) and to Template 2 family (Figure 5b). The waveform of an event j is shown with the scaling of equation (15), meaning that inside each family, variations of the average amplitude are variations of $(\Delta\sigma^j)^{4/3}$.

The P high frequency records of events associated with Template 1 show two very distinct behaviors. Template 1 itself and some other events have a clear onset close to the expected P arrival followed by large similar amplitudes. But the majority of events are VLFEs: they do not exhibit any amplitude increase at the P wave arrival and the signals remain at the noise level over the full window. For this specific template (as well as for all the other templates i), an event j is automatically categorized as a VLFE when $\Delta\sigma^j_{m_i}$ is below 0.01, and as a standard earthquake when $\Delta\sigma^j_{m_i}$ is between 0.01 and 1. Based on this criterion, blue and magenta colors in Figure 5a refer to standard earthquakes and VLFEs, respectively. As the P high frequency record of a VLFE j is usually at the noise level, its determined $\Delta\sigma^j_{m_1}$ value is an upper bound of its actual value. Based on the VLFEs with best observation potential (large events occurring in quiet times), the stress drop ratio between VLFEs and energetic standard earthquakes can be inferred to be lower than 10^{-4}.

Among the 49 events associated with Template 1, 34 are VLFEs. Their locations (map inset of Figure 4) show that they all occur to the southeast of Template 1, in an area where associated standard earthquakes are absent.

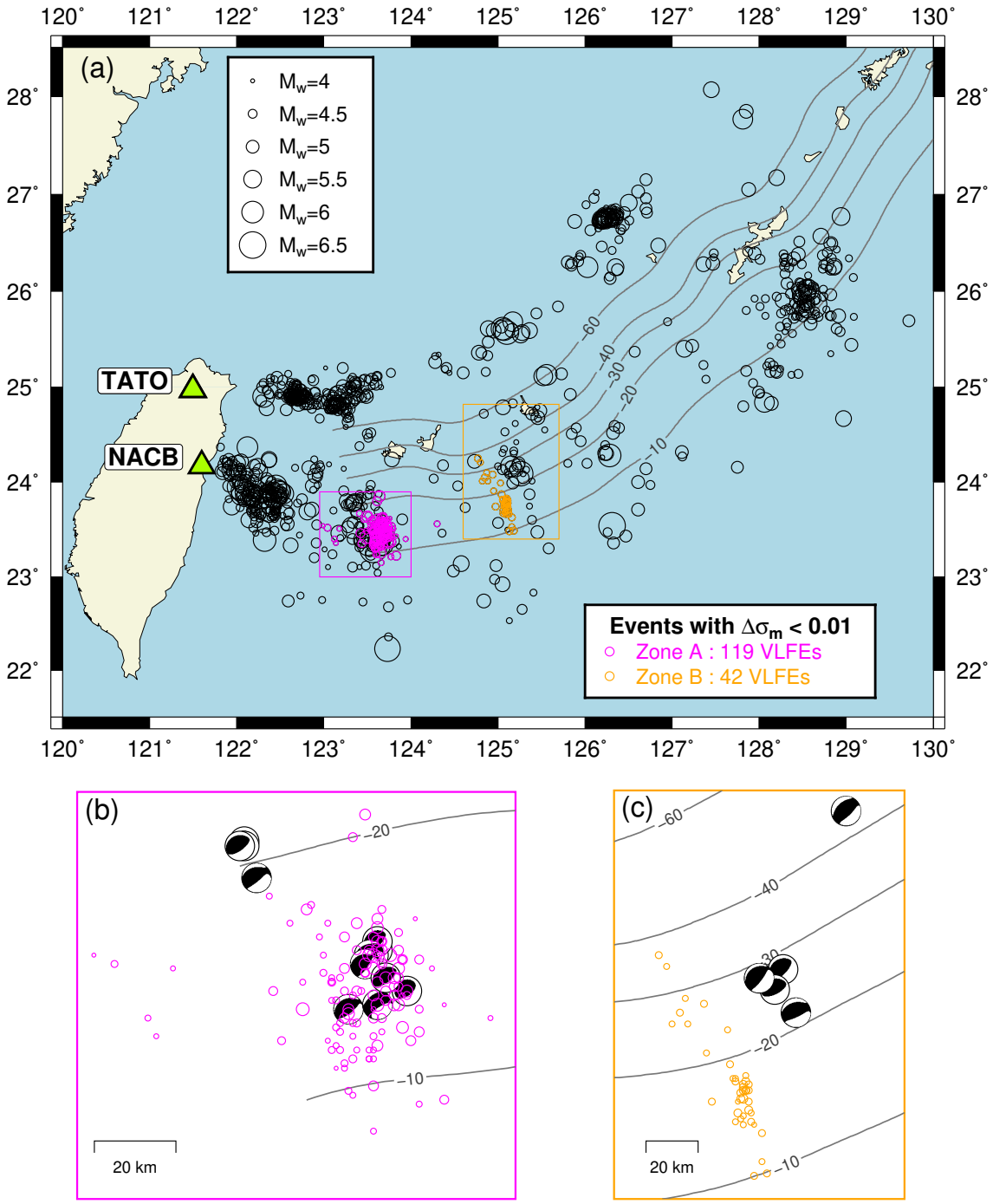

Figure 6 Location of events and VLFEs in the 2004-2024 period. (a) Map showing all the detected and located events (circles sized to the magnitude), using the 289 templates jointly recorded by TATO, INU and NACB stations. 703 events are not present in the original GCMT template catalog. Events j associated with a least one template i such that $\Delta\sigma^j_{m_i}$ <0.01 are colored. These VLFEs occur in two distinct areas hereafter referred to as zone A (magenta) and zone B (orange). (b) Zoom over the VLFEs occurring in zone A. Location and focal mechanisms of all the templates associated with these VLFEs are shown in black. (c) Same as (b) for zone B. Thin grey lines are isodepth contours of the Ryukyu slab according to the Slab1.0 model (Hayes et al., 2012).

As these VLFEs share the focal mechanism of Template 1, they most likely occur on the subduction interface, updip of the seismogenic area. According to Slab1.0 geometry (Hayes et al., 2012), their depths are in the 10–20 km depth range. VLFEs in this area were already detected by Ando et al. (2012) and this VLFE region was referred to the Yaeyama area by Nakamura and Sunagawa (2015). In contrast, no event associated with Template 2 (Figure 5b) displays a VLFE character. The waveforms of all events j have a clear P wave arrival followed by a similar amplitude level, resulting in $\Delta\sigma^j_{m_2}$ >0.01.

4.2 Events location, 2004-2024

The procedure illustrated in section 4.1 is applied to the 289 templates jointly recorded by the three stations. Figure 6a shows the location and magnitude of the detected events, after taking into account the multiple detec-

tions. For an event j that is multiply detected by n templates, its selected location is the one computed from the best correlated template (by means of $\max_{i=1,n} \bar{C}^{ij}$). Its selected magnitude is the median of the n magnitudes computed for each individual template. In total, 992 individual events are relocated among which 703 are not present in the template catalog.

Among these 703 events, 478 can be associated with events of the reviewed ISC catalog (International Seismological Centre, 2024). For origin times, the differences with ISC are -1 s on average with a standard error of 6.1 s. In terms of epicentral location, the average differences in the East and North directions are -3.3 km and -1.8 km, with a standard error of 15.9 km and 21.8 km, respectively. The histograms of these differences are provided in the Supplemental Figure S1. This comparison shows that the event parameters are determined with very little bias compared to catalogs based on first arrivals. In addition, part of the differences are not due to the inaccuracy of the method itself but to the location differences between GCMT locations (used as reference for relocation) and ISC locations.

4.3 Location and mechanism of the very low frequency earthquakes

When an event j is associated with at least one template i for which $\Delta\sigma^j_{m_i}$ <0.01, j is categorized as a VLFE. Figure 6a shows that in most of the study zone, events are standard earthquakes, that only belong to families similar to the one shown in Figure 5b. VLFEs are detected in two specific areas, that we refer to as zone A and zone B. VLFEs detected by Template 1 (section 4.1) belongs to zone A. Zone A is the most active VLFE area with 119 detected and relocated VLFEs, whose moment magnitudes range between 3.96 and 5.01 (Supplementary Table S1). In Figure 6b, these events are shown together with the templates (location and focal mechanisms) that enable their detection. As all such templates have a subduction interplate mechanism, this is also the case for the detected VLFEs. A number of templates take place in the area where most of the VLFEs occur. This is explained by the fact that these templates are in the "SWEQ" category of the GCMT catalog, meaning that they were only detected using their surface wave signals. These templates are therefore themselves VLFEs.

In zone B, 42 VLFEs are detected and relocated, on a narrower magnitude range between 4.11 and 4.51 (Supplementary Table S2). These VLFEs also have a subduction interplate mechanism, based on the templates that detect them (Figure 6c). In this case, the templates are away from the VLFEs locations, and are consistently not referred as "SWEQ" in the GCMT catalog.

None of the 161 VLFEs are present in the ISC catalog (International Seismological Centre, 2024), outside of the few "SWEQ" GCMT events mentioned above. This is a further confirmation that all these VLFEs have a distinct low frequency character that prevented their detection using high-frequency P-waves. According to the Slab1.0 geometry (Hayes et al., 2012) and to the epicentral locations, the majority of the VLFE activity in both zones is consistent with reverse slip on the subduction interface occurring at shallow depths (between 10 km and 20 km).

4.4 Comparison with existing catalogs of very low frequency earthquakes

In the southern Ryukyu subduction zone, three studies (Ando et al., 2012; Nakamura and Sunagawa, 2015; Nakamura and Yakabu, 2025) have provided VLFE catalogs available on the slow earthquake database (Kano et al., 2018). We first focus here on the Ando et al. (2012) and Nakamura and Sunagawa (2015) articles, hereafter referred as A12 and NS15, respectively. Both studies identify VLFEs by first detecting time windows above the background level in the 0.02 Hz–0.05 Hz frequency range, and then keeping only the ones that cannot be associated with classical seismicity. The criteria for this non-association are (1) that the potential events are absent from the local and teleseismic earthquake catalogs and (2) that the highpass filtered (above 1 Hz) records are not typical of missed local earthquakes.

This strategy results in a large number of detected VLFEs in the southern Ryukyu subduction zone, about 600 in 2007 for A12 and about 3000 in 2002-2014 for NS15. The detection number is increased by the fact that both studies use YNG and IGK stations (shown in Figure 7) from the F-Net network (National Research Institute for Earth Science and Disaster Resilience, 2019), located close to the VLFE areas, and therefore able to identify low magnitude VLFEs. These two stations would not have been ideal for the application of the VLFE_DRL method, because rapid Green's functions changes would prevent associating events far enough from their templates. The smaller number of VLFEs detected by the VLFE_DRL method can also be explained by other factors. VLFEs are not detected if they are too far (in terms of location and/or focal mechanism) from the existing templates and they can be missed if two (or more) of them occur within 300 seconds, i.e. within the duration of the template window.

However, even when VLFEs are detected at several stations by the strategy of A12 and NS15, their characteristics (location, magnitude, focal mechanism) remain much more uncertain than for standard earthquakes. NS15 built their VLFE location catalog using the timing of the maximum of the surface wave amplitude together with a constant surface wave velocity, and estimated that the horizontal uncertainty was of the order of 100 km. This explains why a number of VLFEs epicenters are located in unexpected areas (oceanward from the trench or inland Taiwan). Similarly, magnitude uncertainties are likely, as magnitudes come from empirical amplitude relationships at a reference station. For these reasons, A12 discussed the VLFE characteristics only for a small subset of the detected VLFEs, for which a moment tensor solution could be obtained. In this case, location, magnitude, and focal mechanism are much more accurately determined. In the region corresponding to zone A and zone B (and the area in between), about 50 VLFEs are present in the A12 catalog.

Figure 7a shows the comparison between the VLFEs determined here by the VLFE_DRL method (hereafter

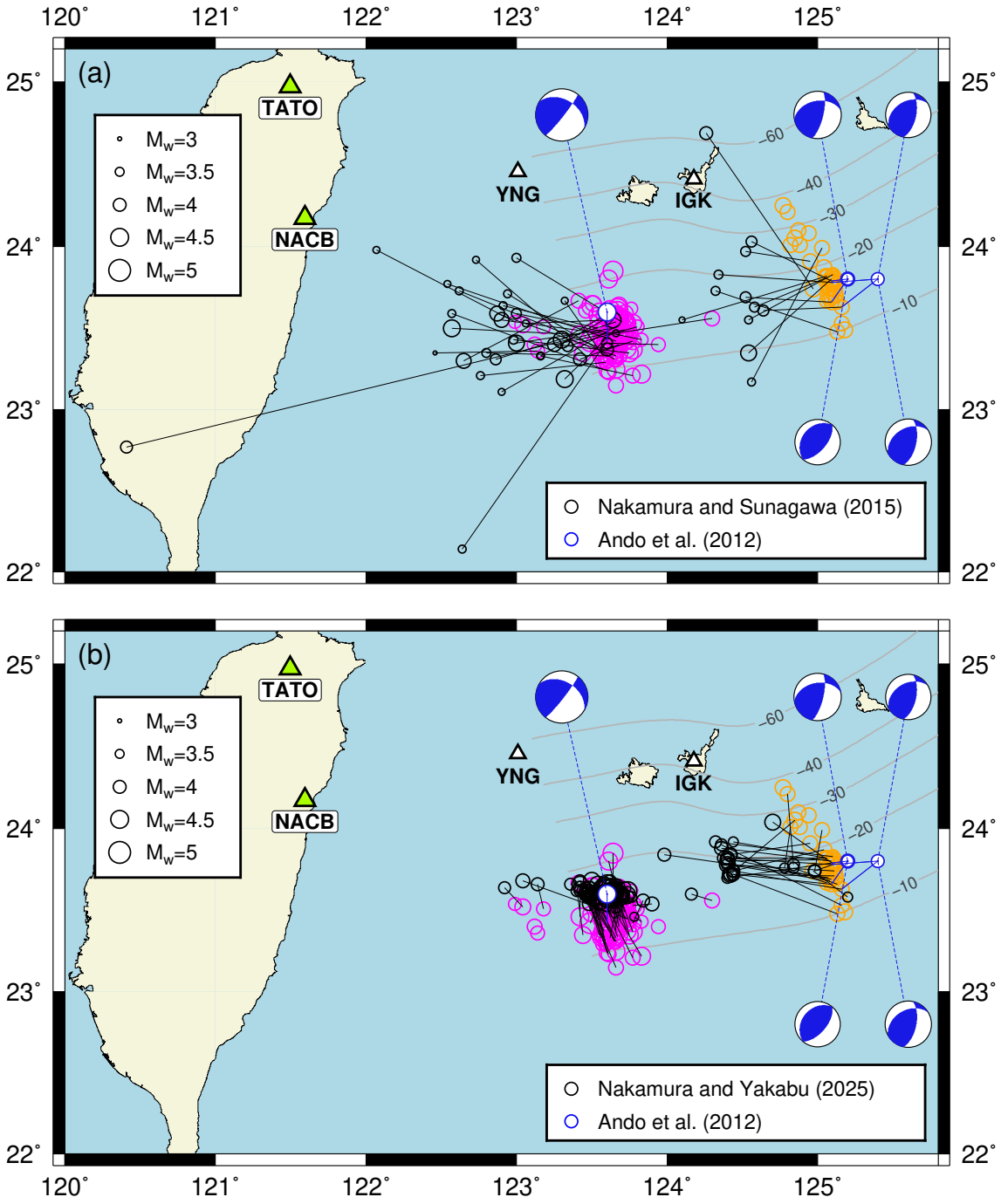

Figure 7 Comparison between the VLFEs characterized in this study and in other catalogs. (a) As in Figure 6, VLFEs of zones A are shown with magenta-contoured circles and VLFEs of zone B are shown with orange-contoured circles. For each of the 47 VLFEs that can be temporally associated with an event from the NS15 catalog (shown in this case by a black-contoured circle), a black line connects the two locations. For each of the 5 VLFEs that can be temporally associated with an event from the A12 catalog (shown in this case by a white-filled blue-contoured circle), a blue line connects the two locations. Dashed blue lines connect the focal mechanisms determined by A12 to their corresponding VLFEs. The size of each circle is scaled to the event magnitude determined by each catalog. YNG and IGK seismic stations, used by A12 and NS15, are shown in addition to the TATO and NACB seismic stations. (b) Same as (a), but showing the comparison with NY25 instead of NS15. 107 VLFE_DRL events can be associated with NY25 events.

referred as VLFE_DRL events) and the VLFEs present in the A12 and NS15 catalogs. An association between a VLFE_DRL event and an A12 (or NS15) event is made if their origin times do not differ by more than 100 s. Even if A12 and NS15 events are more numerous, a significant number of VLFE_DRL events cannot be associated. In the common date ranges, only 47 of the 85 VLFE_DRL events can be associated with NS15 events and only 5 of the 9 VLFE_DRL events can be associated with A12 events. Interestingly, large magnitude VLFE_DRL events (including the largest one that occurred in zone A on 2007/01/18, with a determined magnitude of $M_w = 5.01$) are frequently not associated with A12 nor NS15 events. The most likely explanation is that

the high frequency content of these VLFEs is detectable (even if abnormally low) at the closest YNG or IGK stations. As a result, based on their second criterion, these VLFEs were categorized as local earthquakes by A12 and NS15. We indeed show in Supplemental Figure S2 that a large VLFE does generate a detectable signal at high frequencies at stations YNG and IGK.

The NS15 events are spread out over a larger area compared to the VLFE_DRL events. The former events are also shifted in the West direction, by an average value of $\simeq$70 km. Such a difference is not observed for any of the A12 events, whose moment tensor-based locations are expected to be more precise. Additionally, the relatively small location biases and uncertainties of VLFE_DRL (see section 4.2 and Supplementary Figure S1), especially in the East-West direction, cannot explain this difference.

NS15 events also have a systematic lower moment magnitude compared to the VLFE_DRL events, with an average difference of $\simeq -0.7$. This difference is also observed to a lower extent when comparing the A12 events with the VLFE_DRL events, in which case the average difference is $\simeq -0.3$. Consistently with the VLFE_DRL events (Figure 6), the 5 associated A12 events display a focal mechanism in general agreement with a subduction interplate mechanism.

This comparison first revealed that VLFE_DRL events are clearly less numerous than the A12 and NS15 events. However, their locations and magnitudes are very likely more precise than the ones of the NS15 events, and they are obtained with less effort than the A12 events, which required a moment tensor inversion. Furthermore, the quantitative stress drop comparison included in the VLFE_DRL method offers a more objective tool to detect VLFEs than the direct observation of their high-frequency content. This is a natural explanation of why about half of the VLFE_DRL events, and a significant proportion of the largest ones, are not present in the A12 and NS15 catalogs.

Figure 7b shows the comparison between the VLFE_DRL events and the VLFEs located by Nakamura and Yakabu (2025) (using their catalog referred as FB, ranging from 2000 to 2024). Nakamura and Yakabu (2025), hereafter referred as NY25, used the stations of the BATS network in Taiwan together with stations of the F-Net network (including YNG and IGK), and first determined the source parameters of two VLFEs located in zone A by moment tensor inversion. In a second step, NY25 built their VLFE catalog by using these two events as templates. Among the 161 VLFE_DRL events, 107 can be associated with NY25 events.

In zone A, the VLFE_DRL and NY25 VLFEs are consistently located, which confirms that the NS15 events (Figure 7a) are spread over a too large area. In zone A, the North-South extension of the VLFE cluster is smaller in NY25 than in VLFE_DRL, which can be explained by the denser azimuthal coverage of NY25. However, large location differences between VLFE_DRL and NY25 remain for zone B (not observed between VLFE_DRL and A12), possibly due to the fact that NY25 did not use templates close enough from this area.

4.5 Frequency magnitude distribution of very low frequency earthquakes, 1992-2024

Figure 8a shows the time-magnitude distribution of the VLFEs in zones A and B, in the 2004–2024 time period. Many of the VLFEs appear to be clustered in time, which is consistent with the SSEs external forcing discussed in Nakamura and Sunagawa (2015). Interestingly, if correcting for the suggested $\simeq$70 km westward bias of the NS15 VLFEs, most of them would be located directly updip of the SSEs sources (Heki and Kataoka, 2008; Nishimura, 2014) rather than at their southwestern edges.

Both zones A and B have a well-defined maximum magnitude (4.9–5 for zone A and 4.4–4.5 for zone B). In zone A, 17 VLFEs have a moment magnitude between 4.8 and 5, but none above. Even if absolute magnitude values may be slightly underestimated (down to about -0.2 magnitude units, see section 2.2), this magnitude saturation effect remains. This behavior contrasts with most time-magnitude distributions observed for standard earthquakes, where the determination of the maximum magnitude is itself difficult.

In order to confirm the existence of the maximum magnitude of VLFEs in zone A, the TATO-INU pair is also considered. This enables extending the time period to 1992–2024. All the VLFEs detected with one of the templates shown in Figure 6b are selected. The VLFEs of zone B cannot be properly characterized with TATO station, as the P waves of standard earthquakes are too close from the noise level of the station. Figure 8b shows the observed magnitude distribution for zone A. Some differences with Figure 8a are expected because the higher requested correlation level may lead to reject some events and because the magnitude scaling is only done with two stations. But as in Figure 8a, no VLFEs larger than $M_w = 5$ are detected, and the total number of VLFEs with magnitudes between 4.8 and 5 now reaches 20.

Figure 8c shows the Gutenberg-Richter curves of the VLFEs of zone A (magnitude range of events in zone B is too narrow). Both incremental (linear scale histogram) and cumulative (logarithmic scale) occurrences are shown as a function of M_w. Solid lines refer to the VLFEs located by the three stations TATO,INU and NACB (Figure 8a) and dashed lines to the VLFEs detected by the TATO-INU pair (Figure 8b). The magnitude distributions of VLFEs poorly fits a law where the number of events of magnitude M_w decreases exponentially with M_w. This disagreement is both due to the large number of events of maximum magnitude and to the fact that there is only a modest decrease of the events number as a function of magnitude. Between magnitudes 4.3 and 4.9, the approximate agreement of the cumulative Gutenberg-Richter curve with a linear decay of slope -1 is misleading, as it would predict an unrealistic number of VLFEs above M_w=5.

We finally explore the possibility that VLFEs of larger magnitude are not detected because, due to their potentially very long duration, they are not correlated to any template in the 0.0125–0.03 Hz frequency range. How-

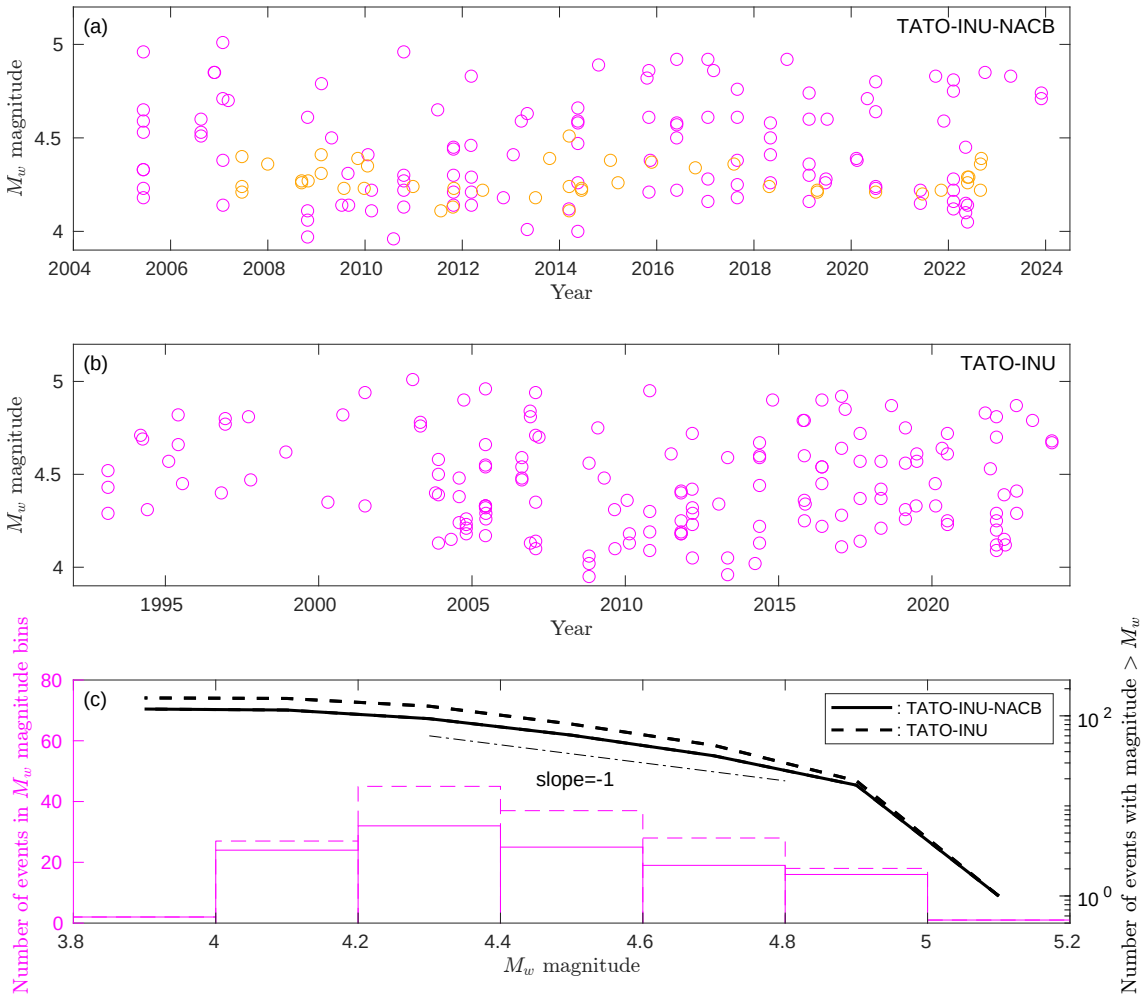

Figure 8 Time-magnitude distribution of VLFEs. (a) Time-magnitude distribution of VLFEs located by the TATO, INU and NACB stations in the 2004–2024 time period. Events shown with magenta and orange colors belong to zones A and B, respectively. Their locations are shown in Figures 6b and 6c. (b) Time-magnitude distribution of VLFEs detected by the TATO-INU pair in the 1992–2024 time period. Only events j of zone A detected with a high correlation ($C_{12}^{ij} \geq 0.8$) and identified as VLFEs using one of the templates i of Figure 6b are considered. (c) Magnitude distribution in incremental form (magenta histogram, linear scale) and cumulative form (black curve, logarithmic scale) of VLFEs in zone A. Solid lines refer to the VLFEs located by the TATO, INU, and NACB stations (a) and dashed lines to the VLFEs detected by the TATO-INU pair (b). The dashdotted line indicates the -1 slope ("b-value") classically observed in seismicity catalogs.

ever, search for VLFEs in the 0.01–0.02 Hz frequency range did not reveal any VLFEs with magnitude larger than 5.

5 Discussion and conclusion

The VLFE_DRL method developed here enables the enrichment of existing seismicity catalogs, by detecting, characterizing, and locating events in the vicinity of cataloged earthquakes. The final high frequency characterization determines whether all the detected events follow the same moment-dependent high frequency emission. This approach is therefore suitable to document VLFEs located in the neighborhood of standard earthquakes.

The application of the method to the southern Ryukyu subduction zone – where VLFEs have been previously detected (Ando et al., 2012; Nakamura and Sunagawa, 2015; Nakamura and Yakabu, 2025) – reveals several of its advantages. First, all detected VLFEs have a known focal mechanism (the one of their template) and moment magnitude (obtained by amplitude ratio). Second, the VLFE location, obtained relatively to a standard earthquake, is very likely to be more precise (at least when the VLFEs are detected from three well-different azimuths) than methods based on envelope picking. Finally, the spectral differences between earthquakes and VLFEs are quantified in terms of equivalent stress drop ratio. When computed between energetic earthquakes and VLFEs, this ratio is shown to reach at least 10000.

In the southern Ryukyu subduction zone, all detected VLFEs are consistent with reverse slip episodes occurring on or close to the subduction interface. Compared with classical interplate seismicity, VLFEs occur closer to the trench, and no area shows a mixed behavior with both VLFEs and standard earthquakes. In the two identified VLFE zones, the events can then be understood to activate friction-specific patches, that are unable to generate standard earthquakes of significant magnitude. Models introducing a rate strengthening friction law,

with or without the inclusion of local strong patches, were shown to reproduce this behaviour (Nakata et al., 2011; Wu et al., 2019).

Future applications of the VLFE_DRL method can be made in numerous places of the world where some seismic events have likely been missed due to sparse local instrumentation. In its present form, the method can only detect and locate events similar to past earthquakes, in terms of focal mechanism, depth, and relative location. This limitation can, however, be relaxed by the use of synthetic templates, as in the study of Baba et al. (2021). As the VLFE_DRL method can detect events not collocated with their templates, the spatial gridding of the synthetic templates can be made coarser with respect to standard template matching approaches. The event search is thus made more efficient, which enables the exploration of broader areas and increases the likelihood of detecting new exotic events hidden in the continuous seismic waveforms.

Acknowledgements

We are grateful to the long-term engineering efforts made to install and maintain high-quality broadband seismic sensors, and to publicly distribute the associated data. We thank the two anonymous reviewers for their comments and advice which helped to improve the original manuscript. We thank Léonard Seydoux, Pascal Bernard, and Claudio Satriano for discussion on the method and/or on the process of very low frequency earthquakes. The SAC (http://ds.iris.edu/ds/nodes/dmc/software/downloads/sac/) free software was used for data processing and the GMT (https://www.generic-mapping-tools.org/) free software was used for maps. Numerical computations were performed on the S-CAPAD/DANTE platform, IPGP, France.

Data and code availability

Seismic data are publicly available and are part of the Federation of Digital Seismograph Networks (FDSN). The citations of the corresponding networks have been included in the main text and thus appear in the references. Seismic data and metadata were accessed using FDSN webservices implemented at the SAGE/Earthscope data center (http://ds.iris.edu/ds/nodes/dmc/), at the IPGP data center (http://datacenter.ipgp.fr/) and at the Epos-France data center (https://ws.resif.fr/). F-Net data were retrieved on the webpage https://www.fnet.bosai.go.jp. The GCMT catalog (ndk format) is publicly available at the GCMT website (https://www.globalcmt.org/CMTfiles.html). VLFE catalogs were retrieved on the webpage on the slow earthquake database (http://www-solid.eps.s.u-tokyo.ac.jp/~sloweq/, supported by JSPS KAKENHI Grant Number JP21H05200 and JP16H06472. The VLFE_DRL code is available in a Zenodo repository (Vallée and Delaporte, 2025).

Competing interests

The authors have no competing interests.

References

Aki, K. Scaling law of seismic spectrum. *Journal of Geophysical Research*, 72(4):1217–1231, Feb. 1967. doi: 10.1029/jz072i004p01217.

Albuquerque Seismological Laboratory/USGS. Global Seismograph Network (GSN - IRIS/USGS), 1988. doi: 10.7914/SN/IU.

Allmann, B. P. and Shearer, P. M. Global variations of stress drop for moderate to large earthquakes. *Journal of Geophysical Research: Solid Earth*, 114(B1), Jan. 2009. doi: 10.1029/2008jb005821.

Ando, M., Tu, Y., Kumagai, H., Yamanaka, Y., and Lin, C. Very low frequency earthquakes along the Ryukyu subduction zone. *Geophysical Research Letters*, 39(4), Feb. 2012. doi: 10.1029/2011gl050559.

Asano, Y., Obara, K., and Ito, Y. Spatiotemporal distribution of very-low frequency earthquakes in Tokachi-oki near the junction of the Kuril and Japan trenches revealed by using array signal processing. *Earth, Planets and Space*, 60(8):871–875, Aug. 2008. doi: 10.1186/bf03352839.

Baba, S., Obara, K., Takemura, S., Takeo, A., and Abers, G. A. Shallow Slow Earthquake Episodes Near the Trench Axis off Costa Rica. *Journal of Geophysical Research: Solid Earth*, 126(9), Sept. 2021. doi: 10.1029/2021jb021706.

Bird, P. An updated digital model of plate boundaries. *Geochemistry, Geophysics, Geosystems*, 4(3), Mar. 2003. doi: 10.1029/2001gc000252.

Boore, D. M. Stochastic simulation of high-frequency ground motions based on seismological models of the radiated spectra. *Bulletin of the Seismological Society of America*, 73(6A): 1865–1894, 1983. doi: 10.1785/BSSA07306A1865.

Chounet, A. and Vallée, M. Global and Interregion Characterization of Subduction Interface Earthquakes Derived From Source Time Functions Properties. *Journal of Geophysical Research: Solid Earth*, 123(7):5831–5852, July 2018. doi: 10.1029/2018jb015932.

Ekstrom, G. Global Detection and Location of Seismic Sources by Using Surface Waves. *Bulletin of the Seismological Society of America*, 96(4A):1201–1212, Aug. 2006. doi: 10.1785/0120050175.

Ekström, G. A global model of Love and Rayleigh surface wave dispersion and anisotropy, 25-250 s. *Geophysical Journal International*, 187(3):1668–1686, Oct. 2011. doi: 10.1111/j.1365-246x.2011.05225.x.

Ekström, G., Nettles, M., and Dziewoński, A. The global CMT project 2004–2010: Centroid-moment tensors for 13,017 earthquakes. *Physics of the Earth and Planetary Interiors*, 200–201:1–9, June 2012. doi: 10.1016/j.pepi.2012.04.002.

Fan, W., Barbour, A. J., McGuire, J. J., Huang, Y., Lin, G., Cochran, E. S., and Okuwaki, R. Very Low Frequency Earthquakes in Between the Seismogenic and Tremor Zones in Cascadia? *AGU Advances*, 3(2), Mar. 2022. doi: 10.1029/2021av000607.

Frechet, J. *Sismogenese et doublets sismiques*. PhD thesis, Universite Scientifique et Medicale de Grenoble, 1985.

Ghosh, A., Huesca-Pérez, E., Brodsky, E., and Ito, Y. Very low frequency earthquakes in Cascadia migrate with tremor. *Geophysical Research Letters*, 42(9):3228–3232, May 2015. doi: 10.1002/2015gl063286.

Gibbons, S. J. and Ringdal, F. The detection of low magnitude seismic events using array-based waveform correlation. *Geophysical Journal International*, 165(1):149–166, Apr. 2006. doi: 10.1111/j.1365-246x.2006.02865.x.

Guo, H. and Zhang, H. Development of double-pair double difference earthquake location algorithm for improving earthquake

locations. *Geophysical Journal International*, 208(1):333–348, Oct. 2016. doi: 10.1093/gji/ggw397.

Hayes, G. P., Wald, D. J., and Johnson, R. L. Slab1.0: A three-dimensional model of global subduction zone geometries. *Journal of Geophysical Research: Solid Earth*, 117(B1), Jan. 2012. doi: 10.1029/2011jb008524.

Heki, K. and Kataoka, T. On the biannually repeating slow-slip events at the Ryukyu Trench, southwestern Japan. *Journal of Geophysical Research: Solid Earth*, 113(B11), Nov. 2008. doi: 10.1029/2008jb005739.

Hutchison, A. A. and Ghosh, A. Very low frequency earthquakes spatiotemporally asynchronous with strong tremor during the 2014 episodic tremor and slip event in Cascadia. *Geophysical Research Letters*, 43(13):6876–6882, July 2016. doi: 10.1002/2016gl069750.

Ide, S. Characteristics of slow earthquakes in the very low frequency band: Application to the Cascadia subduction zone. *Journal of Geophysical Research: Solid Earth*, 121(8):5942–5952, Aug. 2016. doi: 10.1002/2016jb013085.

Ide, S., Beroza, G. C., Shelly, D. R., and Uchide, T. A scaling law for slow earthquakes. *Nature*, 447(7140):76–79, May 2007. doi: 10.1038/nature05780.

Institut de physique du globe de Paris (IPGP) and École et Observatoire des sciences de la Terre de Strasbourg (EOST). GEOSCOPE, French Global Network of broad band seismic stations, 1982. doi: 10.18715/GEOSCOPE.G.

Institute of Earth Sciences, Academia Sinica, Taiwan. Broadband Array in Taiwan for Seismology, 1996. doi: 10.7914/SN/TW.

International Seismological Centre. On-line Bulletin. doi: 10.31905/d808b830.

Ishihara, Y. Major existence of very low frequency earthquakes in background seismicity along subduction zone of south-western Japan. In *AGU Fall Meeting Abstracts*, volume 2003, pages S41C–0107, 2003.

Kano, M., Aso, N., Matsuzawa, T., Ide, S., Annoura, S., Arai, R., Baba, S., Bostock, M., Chao, K., Heki, K., Itaba, S., Ito, Y., Kamaya, N., Maeda, T., Maury, J., Nakamura, M., Nishimura, T., Obana, K., Ohta, K., Poiata, N., Rousset, B., Sugioka, H., Takagi, R., Takahashi, T., Takeo, A., Tu, Y., Uchida, N., Yamashita, Y., and Obara, K. Development of a Slow Earthquake Database. *Seismological Research Letters*, 89(4):1566–1575, June 2018. doi: 10.1785/0220180021.

Masse, R. and Needham, R. NEIC-The national earthquake information center. *Earthquakes & Volcanoes (USGS)*, 21(1):4–44, 1989.

Maury, J., Ide, S., Cruz-Atienza, V. M., Kostoglodov, V., González-Molina, G., and Pérez-Campos, X. Comparative study of tectonic tremor locations: Characterization of slow earthquakes in Guerrero, Mexico. *Journal of Geophysical Research: Solid Earth*, 121(7):5136–5151, July 2016. doi: 10.1002/2016jb013027.

Nakamura, M. and Sunagawa, N. Activation of very low frequency earthquakes by slow slip events in the Ryukyu Trench. *Geophysical Research Letters*, 42(4):1076–1082, Feb. 2015. doi: 10.1002/2014gl062929.

Nakamura, M. and Yakabu, R. Spatiotemporal variability and tectonic implications of very low-frequency earthquakes in the southwestern Ryukyu Trench. *Earth, Planets and Space*, 77(1), Nov. 2025. doi: 10.1186/s40623-025-02314-6.

Nakano, M., Hori, T., Araki, E., Kodaira, S., and Ide, S. Shallow very-low-frequency earthquakes accompany slow slip events in the Nankai subduction zone. *Nature Communications*, 9(1), Mar. 2018. doi: 10.1038/s41467-018-03431-5.

Nakata, R., Ando, R., Hori, T., and Ide, S. Generation mechanism of slow earthquakes: Numerical analysis based on a dynamic model with brittle-ductile mixed fault heterogeneity. *Journal of Geophysical Research*, 116(B8), Aug. 2011. doi: 10.1029/2010jb008188.

National Research Institute for Earth Science and Disaster Resilience. NIED F-net [Dataset], 2019. doi: 10.17598/NIED.0005.

Nishimura, T. Short-term slow slip events along the Ryukyu Trench, southwestern Japan, observed by continuous GNSS. *Progress in Earth and Planetary Science*, 1(1), Oct. 2014. doi: 10.1186/s40645-014-0022-5.

Obara, K. and Ito, Y. Very low frequency earthquakes excited by the 2004 off the Kii peninsula earthquakes: A dynamic deformation process in the large accretionary prism. *Earth, Planets and Space*, 57(4):321–326, Apr. 2005. doi: 10.1186/bf03352570.

Peng, Z. and Gomberg, J. An integrated perspective of the continuum between earthquakes and slow-slip phenomena. *Nature Geoscience*, 3(9):599–607, Aug. 2010. doi: 10.1038/ngeo940.

Peng, Z. and Zhao, P. Migration of early aftershocks following the 2004 Parkfield earthquake. *Nature Geoscience*, 2(12):877–881, Nov. 2009. doi: 10.1038/ngeo697.

Poli, P. Continuation of Events Detection with Global Long-Period Seismic Data: An Analysis from 2010 to 2022. *Seismological Research Letters*, 95(3):1486–1494, Aug. 2023. doi: 10.1785/0220230148.

Saffer, D. M. and Wallace, L. M. The frictional, hydrologic, metamorphic and thermal habitat of shallow slow earthquakes. *Nature Geoscience*, 8(8):594–600, July 2015. doi: 10.1038/ngeo2490.

Shelly, D. R., Beroza, G. C., and Ide, S. Non-volcanic tremor and low-frequency earthquake swarms. *Nature*, 446(7133):305–307, Mar. 2007. doi: 10.1038/nature05666.

Takemura, S., Hamada, Y., Okuda, H., Okada, Y., Okubo, K., Akuhara, T., Noda, A., and Tonegawa, T. A review of shallow slow earthquakes along the Nankai Trough. *Earth, Planets and Space*, 75(1), Oct. 2023. doi: 10.1186/s40623-023-01920-6.

Tang, C., Peng, Z., Chao, K., Chen, C., and Lin, C. Detecting low-frequency earthquakes within non-volcanic tremor in southern Taiwan triggered by the 2005 Mw8.6 Nias earthquake. *Geophysical Research Letters*, 37(16), Aug. 2010. doi: 10.1029/2010gl043918.

Vallée, M. and Delaporte, T. VLFE_DRL, 2025. doi: 10.5281/ZENODO.16903906.

Waldhauser, F. and Ellsworth, W. L. A Double-Difference Earthquake Location Algorithm: Method and Application to the Northern Hayward Fault, California. *Bulletin of the Seismological Society of America*, 90(6):1353–1368, Dec. 2000. doi: 10.1785/0120000006.

Walter, W. R., Yoo, S., Mayeda, K., and Gök, R. Earthquake stress via event ratio levels: Application to the 2011 and 2016 Oklahoma seismic sequences. *Geophysical Research Letters*, 44(7):3147–3155, Apr. 2017. doi: 10.1002/2016gl072348.

Wu, B., Oglesby, D. D., Ghosh, A., and Li, B. A Dynamic Rupture Source Model for Very Low-Frequency Earthquake Signal Without Detectable Nonvolcanic Tremors. *Geophysical Research Letters*, 46(21):11934–11943, Nov. 2019. doi: 10.1029/2019gl084135.

Yang, H., Zhu, L., and Chu, R. Fault-Plane Determination of the 18 April 2008 Mount Carmel, Illinois, Earthquake by Detecting and Relocating Aftershocks. *Bulletin of the Seismological Society of America*, 99(6):3413–3420, Nov. 2009. doi: 10.1785/0120090038.

Zhang, M. and Wen, L. An effective method for small event detection: Match and locate (M&L). *Geophysical Journal International*, 200(3):1523–1537, Feb. 2015. doi: 10.1093/gji/ggu466.